Power Decoupling Control of Single-Phase Differential Cuk Inverters

Yujie Hao, Hanbing Dan, *Senior Member, IEEE*, Yao Sun, *Member, IEEE*, Shiming Xie, Wenjing Xiong, *Member, IEEE*, and Mei Su, *Member, IEEE*

***Abstract*—The single-phase differential Cuk inverter (DCI) is a single-stage inverter that offers numerous benefits over other single-stage topologies, making it a promising solution in new energy applications. However, the second-order ripple power inherent in its dc side seriously affects the performance of the system and restricts the application of the DCI. To address this issue, this study presents a novel automatic power decoupling (APD) control method for the DCI. It directly regulates the input current through a feedback linearization-based decoupling control strategy. An impedance-based stability analysis is performed on the DCI under the proposed APD control method. A hardware prototype is built to verify the effectiveness of the proposed control strategy. Experimental results demonstrate that the proposed APD strategy effectively suppresses 97.8% of the second-order ripple in the input current and improves the system efficiency by approximately 2.8%.**

***Index Terms*—Active power decoupling, differential Cuk inverter, single-phase, stability analysis.**

NOMENCLATURE

L_1 and L_2	Input inductors and output inductors.
C_1 and C_2	Blocking capacitors and output capacitors.
$i_{L1(2)}$ and $i'_{L1(2)}$	Inductor currents in Cuk module 1 and 2.
$u_{c1(2)}$ and $u'_{c1(2)}$	Capacitor voltages in Cuk module 1 and 2.
d_1, d_2	Duty cycles of switches S_1 and S_3.
E	DC-link voltage.
u_o and i_o	Output voltage and current.
R	Load resistance.
$PI\,(s)$	Proportional-integral controller.
$PR\,(s)$	Proportional-resonant controller.
$G_{nf}\,(s)$	Transfer function of the notch filter.
$\boldsymbol{Z_o}$	Impedance model of the DCI with power decoupling control.
$\boldsymbol{Y}$	Admittance matrix of the load subsystem.
DPD	Direct power decoupling.
APD	Automatic power decoupling.

Superscript

$\sim$	Small-signal quantities.
-	Steady-state quantities.

Subscript

Σ	Common-mode variables.
Δ	Differential-mode variables.

Received 20 June 2025; revised 11 July 2025; accepted 23 July 2025. Date of publication 28 July 2025; date of current version 8 September 2025. This work was supported in part by the National Natural Science Foundation of China under Grant 62125308, Grant 52337008, Grant 52277071, and Grant U24A20157, and in part by the Hunan Provincial Natural Science Foundation of China under Grant 2024JJ1011. Recommended for publication by Associate Editor H. H.-C. Iu. *(Corresponding authors: Yao Sun; Hanbing Dan.)*

The authors are with the School of Automation, Central South University and with Hunan Provincial Key Laboratory of Power Electronics Equipment and Grid, Changsha 410083, China (e-mail: 244607003@csu.edu.cn; hanbingdan@csu.edu.cn; yaosun@csu.edu.cn; shimingxie@csu.edu.cn; xiongwj@csu.edu.cn; sumeicsu@csu.edu.cn).

Color versions of one or more figures in this article are available at https://doi.org/10.1109/TPEL.2025.3593303.

Digital Object Identifier 10.1109/TPEL.2025.3593303

I. INTRODUCTION

WITH the rapid growth and widespread adoption of clean energy, single-phase inverters are playing an increasingly vital role in new energy generation and energy storage. However, for renewable energy applications such as photovoltaic [1] and fuel-cell systems [2] and the energy sources may fluctuate widely [3]. To ensure voltage compatibility, a dc–dc converter with buck–boost capability is typically required to form a two-stage inverter with the H-bridge inverter [4]. As a result, this cascading operation increases the complexity of the system, leading to additional power loss and reduced power density.

Alternatively, differential inverters, a category of single-stage inverters, is an effective solution to the aforementioned issue. These inverters are classified into the buck, boost, or buck–boost types [5], [6], [7], [8], [9], [10], and are characterized by their compact size and higher power density compared to two-stage inverters [11]. The differential Cuk inverter is a single-phase, single-stage buck–boost inverter, which offers several valuable advantages. For example, it supports both voltage step-up and step-down functionalities, as well as bidirectional power flow [12]. Compared to other types of differential inverters, the differential Cuk inverter (DCI) includes more passive components, potentially affecting its power density. However, the inherent continuity of input and output currents in the DCI eliminates the need for additional filters. As a result, the DCI remains competitive in practical applications despite its higher component count. Therefore, the DCI is a low-cost, high-power density single-stage inverter with significant research and application potential.

Current research on single-phase DCI primarily focuses on modulation methods and control strategies. The commonly used modulation technique for DCI is the continuous modulation scheme (CMS) [13], [14], [15] and the discontinuous modulation scheme (DMS) [12], [16]. Although the use of DMS improves

efficiency compared to CMS, it introduces additional nonlinearities due to topological switching [12]. The nonlinearity problem has been addressed using harmonic-compensation-based control and static-feedback-linearization-based control [16]. Besides, an adaptive modular control method of isolated DCI is designed [17]. This method can address the inherent nonlinearities of DCI using a DMS-based approach while ensuring asymptotic stability and convergence during transient processes. Furthermore, regarding the control method for DCI, a peak-current-based control is applied [18], providing better stability and faster response compared to traditional voltage-mode control. In [19], an optimal switching-sequence-based control method is proposed, offering improved response to large signal disturbances and guaranteeing the stability and robustness of DCI.

However, all the aforementioned research primarily focuses on the output voltage control of DCI. Like the other single-phase inverters, the inherent second-order ripple power in single-phase DCI cannot be overlooked. As is well known, second-order ripple power can adversely affect the performance of single-phase inverters [20], [21]. To address this challenge, active power decoupling is proven to be an effective solution [22]. It is generally implemented by adding decoupling circuits that include switching devices and energy storage components [23]. However, these auxiliary circuits will impact the power density, cost, and efficiency of the converter [24]. Fortunately, by using a well-designed control strategy, differential inverters can achieve active power decoupling without requiring additional circuits [25]. Several single-phase differential inverter topologies and their power decoupling control techniques are comprehensively summarized in [24].

Recent studies have explored diverse power decoupling strategies for differential inverters, such as the direct power decoupling (DPD) method that directly controls the ripple power and the automatic power decoupling (APD) method that regulates the ac and dc power [26]. In [27], a rule-based DPD controller is proposed to reduce second-order ripple current in differential boost inverter. However, this method significantly increases the complexity and computational load of the system. In [28], fractional-order virtual impedance control is proposed for a differential boost inverter, where fractional-order filters are employed to enhance dynamic performance and system stability. However, the fractional order controller is challenging to implement and increases the computational burden. Li et al. [29] introduces a nonlinear power decoupling control scheme using input–output linearization for a single-phase differential grid-tied buck inverter. This approach can be regarded as a DPD method since the ripple power reference is obtained by an extended observer. Additionally, a partial feedback linearization method is applied to the grid-tied differential boost inverter in [30], resulting in an excellent dynamic response in the power decoupling control loop. However, it is difficult to directly apply the above methods to the DCI, as it is a complicated eighth-order nonlinear system.

To ensure good dynamic and steady-state performance of the DCI while suppressing the second-order ripple power at the dc input side, a novel automatic power decoupling control scheme is proposed. The main contributions are as follows.

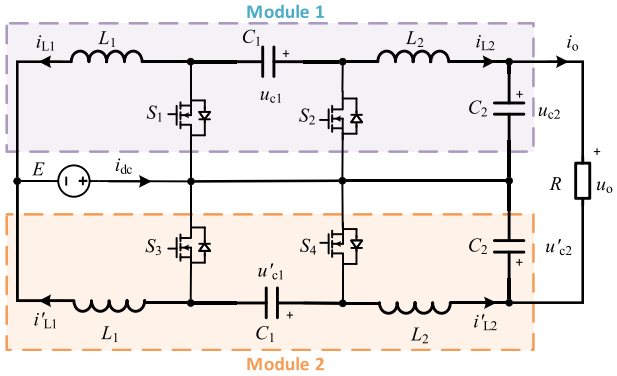

Fig. 1. Circuit topology of the single-phase DCI.

1) An APD control strategy is proposed for the DCI. Not only power decoupling is well realized but also the efficiency of this converter is improved under the proposed control strategy.
2) The impedance model of DCI considering the frequency coupling effects is established. The stability analysis is conducted based on the impedance model, which provides guidelines for controller parameter selection.

The rest of this article is organized as follows. Section II presents the circuit structure of the DCI, along with its average model, and steady-state analysis. Section III provides a detailed discussion of the proposed power decoupling control method. In Section IV, the effectiveness of the proposed method is verified through experiments. Finally, Section V concludes this article.

II. Circuit Modeling and Analysis

A. Circuit Topology

Fig. 1 shows the circuit of single-phase DCI. It is composed of two identical dc–dc Cuk converter modules, each containing two inductors (L_1, L_2) and two capacitors (C_1, C_2). The DCI requires four power switches S_1–S_4, and the switches (S_1, S_2) and (S_3, S_4) in the same Cuk module are fed with complementary gating signals.

B. Average Model of DCI

Assuming that the DCI is operating in continuous current mode. According to Fig. 1, the average model of Cuk module 1 is represented as follows:

$$\begin{cases} L_1 \frac{di_{L1}}{dt} = E - (1-d_1)u_{c1} \\ C_1 \frac{du_{c1}}{dt} = -d_1 i_{L2} + (1-d_1) i_{L1} \\ L_2 \frac{di_{L2}}{dt} = d_1 u_{c1} - u_{c2} \\ C_2 \frac{du_{c2}}{dt} = i_{L2} - i_o \end{cases} \tag{1}$$

where i_{L1} and i_{L2} are the currents flowing through the inductors L_1 and L_2. u_{c1} and u_{c2} are the voltages across the capacitors C_1 and C_2, respectively. d_1 is the duty cycle of the switch S_1.

Similarly, the model of module 2 is given as

$$\begin{cases} L_1 \frac{di'_{L1}}{dt} = E - (1-d_2)u'_{c1} \\ C_1 \frac{du'_{c1}}{dt} = -d_2 i'_{L2} + (1-d_2) i'_{L1} \\ L_2 \frac{di'_{L2}}{dt} = d_2 u'_{c1} - u'_{c2} \\ C_2 \frac{du'_{c2}}{dt} = i'_{L2} + i_o \end{cases} \tag{2}$$

where i'_{L1}, i'_{L2}, u'_{c1}, and u'_{c2} are the currents and voltages in module 2. d_2 is the duty cycle of the switch S_3.

In addition, the output voltage and current are expressed by

$$\begin{cases} u_o = u_{c2} - u'_{c2} \\ i_o = u_o / R \end{cases} \tag{3}$$

C. Model Transformation

To facilitate controller design, the following coordinate transformations are introduced [29]:

$$\begin{bmatrix} x_\Delta \\ x_\Sigma \end{bmatrix} = \begin{bmatrix} 1 & -1 \\ 1 & 1 \end{bmatrix} \begin{bmatrix} x \\ x' \end{bmatrix} \tag{4}$$

where the variables with subscripts Δ and Σ represent the differential-mode (DM) and common-mode (CM) state variables, respectively. x and x' represent the state variables or duty cycles of modules 1 and 2 mentioned above.

After coordinate transformations, the average models of DM and CM are derived as

$$L_1 \frac{di_{\Delta 1}}{dt} = \frac{1}{2}(d_\Delta u_{\Sigma 1} + d_\Sigma u_{\Delta 1}) - u_{\Delta 1} \tag{5.a}$$

$$C_1 \frac{du_{\Delta 1}}{dt} = i_{\Delta 1} - \frac{1}{2}(d_\Delta i_{\Sigma 1} + d_\Sigma i_{\Delta 1}) - \frac{1}{2}(d_\Delta i_{\Sigma 2} + d_\Sigma i_{\Delta 2}) \tag{5.b}$$

$$L_2 \frac{di_{\Delta 2}}{dt} = \frac{1}{2}(d_\Delta u_{\Sigma 1} + d_\Sigma u_{\Delta 1}) - u_{\Delta 2} \tag{5.c}$$

$$C_2 \frac{du_{\Delta 2}}{dt} = i_{\Delta 2} - 2i_o \tag{5.d}$$

and

$$L_1 \frac{di_{\Sigma 1}}{dt} = 2E - u_{\Sigma 1} + \frac{1}{2}(d_\Delta u_{\Delta 1} + d_\Sigma u_{\Sigma 1}) \tag{6.a}$$

$$C_1 \frac{du_{\Sigma 1}}{dt} = i_{\Sigma 1} - \frac{1}{2}(d_\Delta i_{\Delta 1} + d_\Sigma i_{\Sigma 1}) - \frac{1}{2}(d_\Delta i_{\Delta 2} + d_\Sigma i_{\Sigma 2}) \tag{6.b}$$

$$L_2 \frac{di_{\Sigma 2}}{dt} = \frac{1}{2}(d_\Delta u_{\Delta 1} + d_\Sigma u_{\Sigma 1}) - u_{\Sigma 2} \tag{6.c}$$

$$C_2 \frac{du_{\Sigma 2}}{dt} = i_{\Sigma 2} \tag{6.d}$$

It can be seen that the output voltage u_o (equal to $u_{\Delta 2}$) is mainly related to the DM equations of the model. The significant variable $i_{\rm dc}$ (equal to $i_{\Sigma 1}$) is mainly related to the CM equations.

D. Steady-State Analysis

By applying the volt-second balance principle to (5) and (6), the following relationship is obtained:

$$u_{\Delta 1} = u_{\Delta 2} \tag{7}$$

$$u_{\Sigma 1} = u_{\Sigma 2} + 2E \tag{8}$$

As observed, the state variables $u_{\Delta 1}$ and $u_{\Sigma 1}$ are represented by $u_{\Delta 2}$ and $u_{\Sigma 2}$, respectively. Therefore, only the voltage across the two output capacitors C_2 needs to be measured, which results in a reduction of two voltage sensors and, thus, reduces the overall cost.

Assuming that the output voltage u_o and current i_o are as follows:

$$\begin{cases} u_o = U_o \cos \omega_1 t \\ i_o = I_o \cos(\omega_1 t - \varphi) \end{cases} \tag{9}$$

where U_o and I_o denote the amplitude. ω_1 and φ are denoted as angular frequency and power factor angle, respectively. Then, the instantaneous power at the ac output side is given as

$$p_o = u_o i_o = \underbrace{\frac{1}{2} U_o I_o \cos(\varphi)}_{P_{dc}} + \underbrace{\frac{1}{2} U_o I_o \cos(2\omega_1 t - \varphi)}_{p_r} \tag{10}$$

where p_o is the instantaneous power on the ac side, $P_{\rm dc}$ is the average power, and p_r is the second-order pulsating power.

The energy stored in the capacitors is expressed as

$$w_C = \frac{1}{2} C_1 (u_{c1}^2 + u_{c1}'^2) + \frac{1}{2} C_2 (u_{c2}^2 + u_{c2}'^2) \tag{11}$$

where w_C represents the energies stored in the capacitors. Equation (11) is rewritten as follows by the CM and DM state variables:

$$w_C = \frac{1}{4}\left(C_1 u_{\Sigma 1}^2 + C_2 u_{\Sigma 2}^2\right) + \frac{1}{4}(C_1 + C_2) u_{\Delta 2}^2 \tag{12}$$

Similarly, the energy stored in the inductors is

$$w_L = \frac{1}{4}\left(L_1 i_{\Sigma 1}^2 + L_2 i_{\Sigma 2}^2\right) + \frac{1}{4}(L_1 i_{\Delta 1}^2 + L_2 i_{\Delta 2}^2) \tag{13}$$

where w_L represents the energies stored in inductors.

Based on the principle of power balance, the following expression is derived:

$$p_{\rm in} = \frac{dw_C}{dt} + \frac{dw_L}{dt} + P_{dc} + p_r + p_{\rm Loss} \tag{14}$$

where $p_{\rm in} = E \cdot i_{\Sigma 1}$ is the input power. The power loss, denoted as $p_{\rm Loss}$, is approximately a constant value $W_{\rm Loss} = \int p_{\rm loss} dt$ within a line cycle.

To prevent pulsating power from being transmitted to the dc side, the second-order pulsating power should be buffered by capacitors and inductors. Thus, the following equation should be satisfied:

$$\int \left(\frac{dw_C}{dt} + \frac{dw_L}{dt} + p_r \right) dt = 0 \tag{15}$$

Assuming that inductor current and inductance are small. Then, the pulsating power buffered by the inductor is negligible. Therefore, according to (7), (8), and (15), the steady-state value

of $u_{\Sigma 2}$ is given in (16) at the bottom of this page, where K is a constant value to ensure the expression inside the square root in (16) is greater than or equal to zero.On the other hand, K determines the value of the dc component of $u_{\Sigma 2}$. By analyzing the harmonic spectrum of (16), it is found that $u_{\Sigma 2}$ mainly contains harmonic components of frequency $2\omega_1$ and $4\omega_1$.

Moreover, as DCI is comprised of two dc–dc converters, u_{c2} and u'_{c2}must be greater than zero for normal operation. Thus, the constraint of the capacitor voltage is expressed as

$$u_{\Sigma 2} > |u_{\Delta 2}| \tag{17}$$

Therefore, a suitable K should be chosen to satisfy the constraint (17). In addition, a large value of K should be avoided to reduce the voltage stress of the devices.

III. Proposed APD Control Strategy and Stability Analysis

Unlike existing control methods for single-phase DCI, this study aims not only to control the output voltage but also to realize power decoupling. To achieve these objectives, an APD control strategy for DCI is proposed, and the control block diagram is shown in Fig. 2. The details are discussed in the following.

A. Model Simplification

As previously mentioned, the single-phase DCI is a higher-order nonlinear system, which complicates the analysis. To facilitate the controller design, model order reduction is performed. According to the time-scale separation principle [31], since the current control loop is designed much faster than the voltage loop, then the volt-second balance is applied to (5.a) and (6.a), the expressions of duty cycles are solved as

$$d_\Delta = \frac{4Eu_{\Delta 1}}{{u_{\Sigma 1}}^2 - {u_{\Delta 1}}^2} \tag{18}$$

$$d_\Sigma = 2\left(1 - \frac{2Eu_{\Sigma 1}}{{u_{\Sigma 1}}^2 - {u_{\Delta 1}}^2}\right) \tag{19}$$

By substituting (18), (19) into equations (5) and (6), a reduced-order system is expressed as

$$\begin{cases} C_1 \frac{du_{\Delta 1}}{dt} = \frac{2E}{{u_{\Sigma 1}}^2 - {u_{\Delta 1}}^2}(u_{\Sigma 1} i_{\Delta 1} - u_{\Delta 1} i_{\Sigma 1} \\ \qquad + u_{\Sigma 1} i_{\Delta 2} - u_{\Delta 1} i_{\Sigma 2}) - i_{\Delta 2} \\ L_2 \frac{di_{\Delta 2}}{dt} = u_{\Delta 1} - u_{\Delta 2} \\ C_2 \frac{du_{\Delta 2}}{dt} = i_{\Delta 2} - 2i_o \end{cases} \tag{20}$$

$$\begin{cases} C_1 \frac{du_{\Sigma 1}}{dt} = \frac{2E}{{u_{\Sigma 1}}^2 - {u_{\Delta 1}}^2}(u_{\Sigma 1} i_{\Sigma 1} - u_{\Delta 1} i_{\Delta 1} \\ \qquad + u_{\Sigma 1} i_{\Sigma 2} - u_{\Delta 1} i_{\Delta 2}) - i_{\Sigma 2} \\ L_2 \frac{di_{\Sigma 2}}{dt} = u_{\Sigma 1} - u_{\Sigma 2} - 2E \\ C_2 \frac{du_{\Sigma 2}}{dt} = i_{\Sigma 2} \end{cases} \tag{21}$$

B. Output Voltage Control

As seen from (20), $u_{\Delta 2}$ is the output, while $i_{\Delta 1}$ and $i_{\Sigma 1}$ serve as control inputs. Determining which control input to use for regulating $u_{\Delta 2}$ requires careful consideration. To ensure that $u_{\Delta 2}$ can be controlled completely under disturbance, the coefficients associated with the chosen control input must be always greater or less than zero. Since $u_{\Delta 1}$ is a sinusoidal waveform and zero-crossing cannot be avoided, $i_{\Sigma 1}$ cannot be used as the control input to control $u_{\Delta 2}$. The coefficient before $i_{\Delta 1}$ is always greater than zero, so $i_{\Delta 1}$ is chosen. On the other hand, because the coefficient before $i_{\Delta 1}$ is time-varying, a virtual control input is selected as

$$\mu_1 = \frac{2E}{{u_{\Sigma 1}}^2 - {u_{\Delta 1}}^2} \cdot u_{\Sigma 1} i_{\Delta 1} \tag{22}$$

where μ_1 represents the virtual control input.

Since the reference for the output voltage is a sinusoidal signal at line-frequency. To track this reference with zero steady-state error, a proportional-resonant (PR) controller is used, which is defined as

$$PR_1(s) = k_{pr1} + \frac{k_{r1} s}{s^2 + {\omega_1}^2} \tag{23}$$

where k_{pr1} is the proportional gain, and k_{r1} is the gain of the resonant term.

Furthermore, since the (20) includes other disturbances that contain integer harmonics at line-frequency, additional resonant terms are included to compensate for these disturbances and are expressed as follows:

$$R_1(s) = \sum_k \frac{k_{r1-k} s}{s^2 + (k\omega_1)^2} \tag{24}$$

where $k_{r1\text{-}k}$ is the gain of the controller, with k = 3,5,7, ⋯. In this article, setting $k = 3$ can meet the requirements and ensure the quality of the output voltage. Then, the virtual control input is designed as

$$\mu_1 = [PR_1(s) + R_1(s)]\,(u^*_{\Delta 2} - u_{\Delta 2}) \tag{25}$$

According to (22), the reference of $i_{\Delta 1}$ is expressed as

$$i^*_{\Delta 1} = \lambda \mu_1 \tag{26}$$

where $\lambda = ({u_{\Sigma 1}}^2 - {u_{\Delta 1}}^2)/2Eu_{\Sigma 1}$.

$$u_{\Sigma 2} = \frac{1}{C_1 + C_2}\left\{-2C_1 E + 2\sqrt{C_1^2 E^2 - (C_1 + C_2)\left[C_1 E^2 - K + \frac{U_o I_o}{4\omega_1}\sin(2\omega_1 t - \varphi) + (C_1 + C_2)\left(\frac{U_o}{2}\cos\omega_1 t\right)^2\right]}\right\} \tag{16}$$

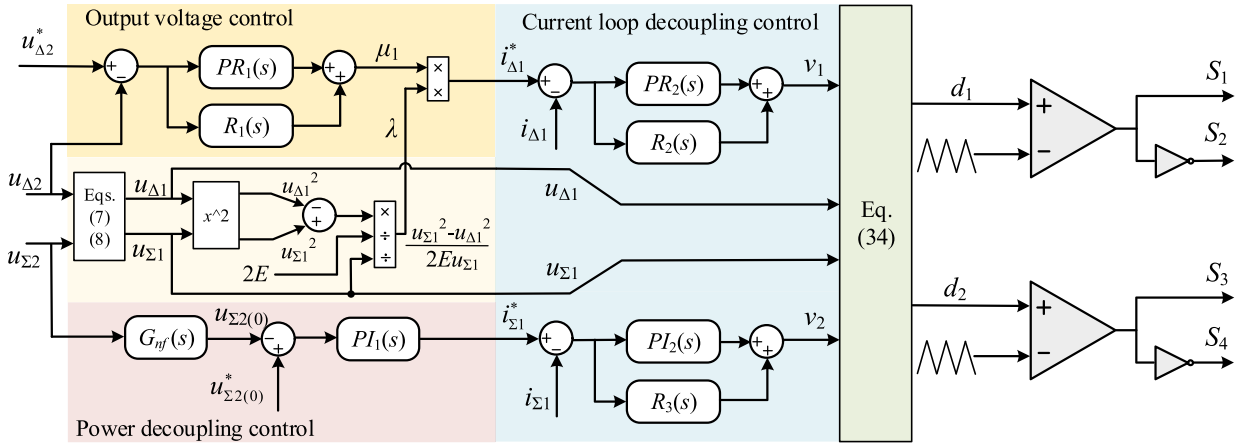

Fig. 2. Block diagram of the proposed APD control strategy for DCI.

C. Power Decoupling Control

The idea of the proposed power decoupling control is to ensure that the reference of $i_{\Sigma 1}$ contains only dc components, while the ripple power is automatically buffered by the capacitors under the APD control approach. To achieve this objective, two important problems should be addressed as follows.

1) How to determine the value of the dc component.
2) How to ensure that the reference of $i_{\Sigma 1}$ does not contain other components.

Recall that the constraint (17) is satisfied by controlling the dc component of $u_{\Sigma 2}$. Therefore, regulating the dc component of $u_{\Sigma 2}$ becomes an implicit control objective. According to (21), it is not difficult to find that the dc component of $i_{\Sigma 1}$ can be used to control the dc component of $u_{\Sigma 2}$. Thus, the output of the controller for the dc component of $u_{\Sigma 2}$ is the reference of $i_{\Sigma 1}$.

Different from the manipulation as shown in (22), a proportional-integral (PI) controller is directly employed to control the dc component of $u_{\Sigma 2}$ and generate the input current reference $i^*_{\Sigma 1}$

$$i^*_{\Sigma 1} = PI_1(s)(u^*_{\Sigma 2(0)} - u_{\Sigma 2(0)}) \tag{27}$$

where $\mathrm{PI}_1(s)$ is expressed as

$$PI_1(s) = k_{p1} + k_{i1}/s \tag{28}$$

where k_{p1} and k_{i1} are the controller gains. $u_{\Sigma 2(0)}$ is the dc component of $u_{\Sigma 2}$ and $u^*_{\Sigma 2(0)}$ is its reference.

To quickly and accurately obtain the dc component of $u_{\Sigma 2}$ is the key to realizing perfect power decoupling. Usually, a low-pass filter is used to extract $u_{\Sigma 2(0)}$. However, there is a tradeoff between extraction accuracy and response speed when using low-pass filters [22]. As mentioned in the steady-state analysis, $u_{\Sigma 2}$ may contain multiple even-order harmonics when power decoupling control is enabled. Therefore, a notch filter tuned at $2\omega_1$ and $4\omega_1$ is applied to extract the average value, with the following transfer function:

$$G_{nf}(s) = \frac{[s^2 + (2\omega_1)^2][s^2 + (4\omega_1)^2]}{[s^2 + 2\xi_1(2\omega_1)s + (2\omega_1)^2][s^2 + 2\xi_2(4\omega_1)s + (4\omega_1)^2]} \tag{29}$$

where ξ_1 and ξ_2 is the damping factor of the notch-filter.

D. Current Loop Decoupling Control

In the previous two sections, the references for the DM and CM currents have been obtained. However, since the actual control inputs of the system are duty cycles, two current control loops are required to regulate the currents $i_{\Delta 1}$ and $i_{\Sigma 1}$, and to determine the duty cycles. From (5.a) and (6.a), it is evident that there are serious couplings between the DM and CM state variables. To simplify the controller design, a decoupling control method based on feedback linearization is applied. Thus, the right-hand sides of (5.a) and (6.a) are treated as single entities and used to regulate the currents $i_{\Delta 1}$ and $i_{\Sigma 1}$, denoted as ν_1 and ν_2

$$\nu_1 = \frac{1}{2}(d_\Delta u_{\Sigma 1} + d_\Sigma u_{\Delta 1}) - u_{\Delta 1} \tag{30}$$

$$\nu_2 = 2E - u_{\Sigma 1} + \frac{1}{2}(d_\Delta u_{\Delta 1} + d_\Sigma u_{\Sigma 1}) \tag{31}$$

Since the reference $i^*_{\Delta 1}$ contains integer harmonics at line-frequency. According to the internal model principle [32], a proportional multiresonant current controller is used to track the current reference. Then, the current controller is designed as follows:

$$\nu_1 = [PR_2(s) + R_2(s)]\,(i^*_{\Delta 1} - i_{\Delta 1}) \tag{32}$$

where $PR_2(s)$ and $R_2(s)$ have the same implementation form as $PR_1(s)$ and $R_1(s)$, respectively.

According to (27), the reference of $i_{\Sigma 1}$ only contains dc components. It seems that only a PI controller is required to ensure that $i_{\Sigma 1}$ accurately tracks the reference without steady-state

error. However, in practice the feedback linearization in (31) is not implemented perfectly due to a delay of one control cycle in digital control. Thus, it is important to include resonance terms $R_3(s)$ with frequencies of 100 Hz and 200 Hz to compensate for these disturbances in the input current. Hence, the controller designed to regulate $i_{\Sigma 1}$ is expressed as follows:

$$\nu_2 = \left[PI_2(s) + R_3(s)\right]\left(i_{\Sigma 1}^{*} - i_{\Sigma 1}\right) \tag{33}$$

where $PI_2(s) = (k_{p2} + k_{i2}/s)$, and k_{p2} and k_{i2} are the controller gains. $R_3(s) = k_{r3\text{-}2}s/[s^2 + (2\omega_1)^2] + k_{r3\text{-}4}s/[s^2 + (4\omega_1)^2]$, and $k_{r3\text{-}2}$ and $k_{r3\text{-}4}$ are the gains of resonant controller at $2\omega_1$ and $4\omega_1$, respectively.

Consequently, combining (30) and (31), the duty cycle d_1 and d_2 are calculated by the following equations:

$$\begin{cases} d_1 = \frac{\nu_1+\nu_2+u_{\Delta 1}+u_{\Sigma 1}-2E}{u_{\Delta 1}+u_{\Sigma 1}} \\ d_2 = \frac{\nu_1-\nu_2+u_{\Delta 1}-u_{\Sigma 1}+2E}{u_{\Delta 1}-u_{\Sigma 1}} \end{cases} \tag{34}$$

To reduce the system cost, $u_{\Delta 1}$ and $u_{\Sigma 1}$ are not directly measured in this study. Instead, (7) and (8) are employed to estimate $u_{\Delta 1}$ and $u_{\Sigma 1}$.

E. Parameter Selection

Output voltage control of DCI is a well-established problem. Thus, this section focuses on the parameter selection rules for the power decoupling controller and current controllers.

For the power decoupling control, to simplify the analysis, the reduced-order model (21) is approximated by treating the terms other than $i_{\Sigma 1}$ as disturbances and approximating the coefficient preceding $i_{\Sigma 1}$ as a constant k_1. Consequently, (21) is equivalent to a linear system, and the transfer function from $i_{\Sigma 1}$ to $u_{\Sigma 2}$ is expressed as

$$G_{pd}(s) = \frac{k_1}{C_1C_2L_2s^3 + (C_1 + C_2)s} \tag{35}$$

Given that the dynamics of the average capacitor voltage are much slower than other parts of the system, the bandwidth of the power decoupling loop in this study is designed to be around $2\omega_1$ with a phase margin exceeding 45°. The corresponding bode diagram is shown in Fig. 3.

For the current control, to satisfy the time-scale separation as previously discussed, the current loops bandwidths are set to be 10 times higher than that of the power decoupling loop. Additionally, to suppress switching noise, the bandwidth is constrained below one-tenth of the switching frequency [33]. Given these considerations, the bandwidths of the DM and CM current loop are set to 2000 Hz to ensure good dynamic response, The bode diagrams are presented in Fig. 4.

F. Stability Analysis

Since the linearized small-signal model of the DCI with power decoupling is a linear time-periodic (LTP) system, the LTP modeling technique is applied to establish a LTP framework-based model for DCI [34]. Additionally, impedance stability criteria based on the determinant is adopted to evaluate the stability of the DCI system with power decoupling [35], [36], [37]. The

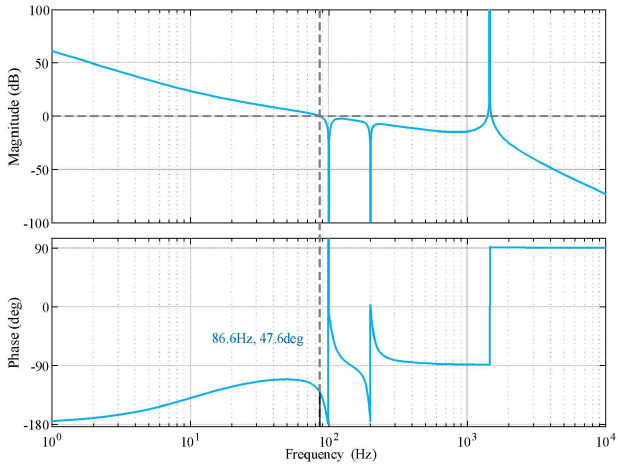

Fig. 3. Bode diagram of the power decoupling loop.

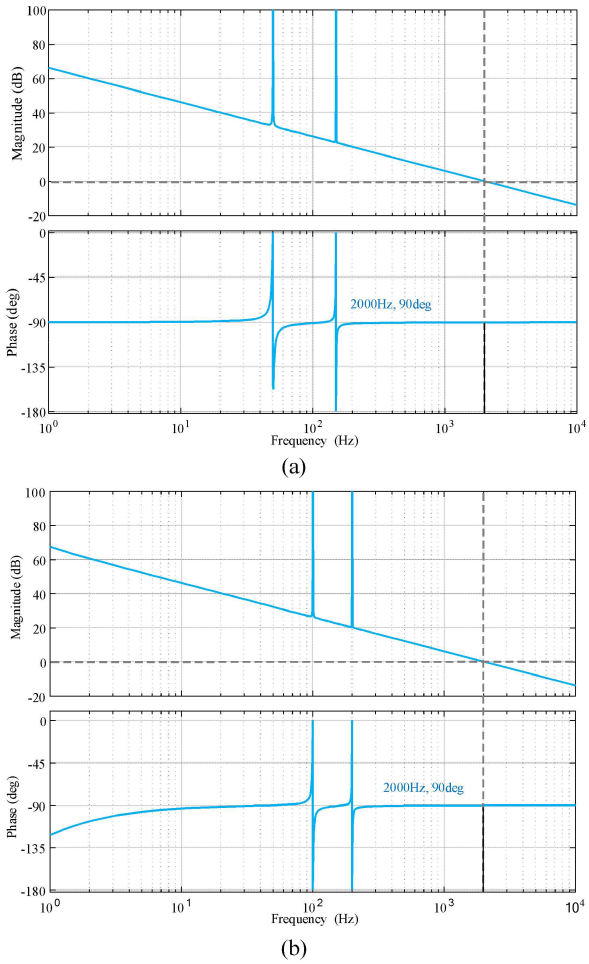

Fig. 4. Bode diagrams. (a) DM current loop. (b) CM current loop.

output impedance matrix of DCI is

$$\tilde{\boldsymbol{u}}_o = \boldsymbol{Z}_o\tilde{\boldsymbol{i}}_o \tag{36}$$

The detailed steps for establishing the impedance model are presented in the Appendix. Additionally, a frequency sweep measurement is performed to verify the correctness of the

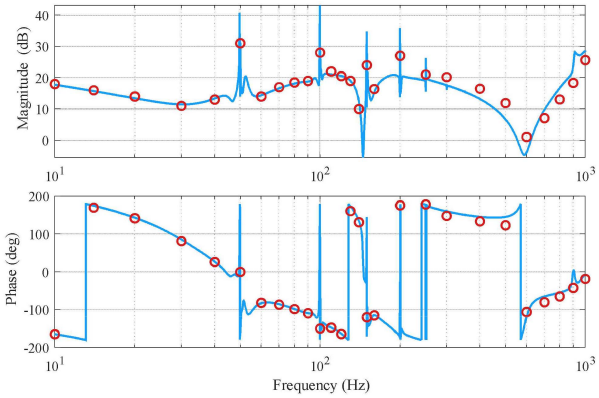

Fig. 5. Bode diagram and simulation measured results of $\boldsymbol{Z}_o(s)$.

TABLE I
CONTROLLER PARAMETERS FOR DIFFERENT CASES

	Power decoupling controller k_{p1} / k_{i1}	Input current controller k_{p2} / k_{i2}
Case 1	0.07 / 5	13 / 50
Case 2	0.105 / 7.24	13 / 50
Case 3	0.07 / 5	9.8 / 34

impedance model. The bode diagram of $\boldsymbol{Z}_o(s)$ and the corresponding measurement results are shown in Fig. 5.

It is observed that the simulation measured results (red dots) closely match the theoretical calculations (blue curve), thereby effectively validating the accuracy of the established impedance model.

Assume that the load subsystem is linear, its admittance matrix is formulated as

$$\tilde{\boldsymbol{i}}_o = \boldsymbol{Y}\tilde{\boldsymbol{u}}_o \tag{37}$$

where $\boldsymbol{Y} = \boldsymbol{I} / R$ is the admittance matrix of the load and $\boldsymbol{I}$ represents a 7×7 identity matrix.

Combining (36) and (37), the closed-loop system of the entire inverter is given as

$$(\boldsymbol{I} - \boldsymbol{Z}_o\boldsymbol{Y})\,\tilde{\boldsymbol{u}}_o = \boldsymbol{0} \tag{38}$$

Stability Criterion: The system is stable if and only if the Nyquist diagram of $\det\{-\boldsymbol{Z}_o\boldsymbol{Y}\}$ does not encircle the point $(-1, j0)$ in the complex plane [37], where $\det\{\cdot\}$ denotes the determinant operation.

Cases 1–3 in Table I are designed to verify the stability analysis of the DCI system. The corresponding Nyquist diagrams are shown in Fig. 6. The stability analysis predicts that the system is stable in Case 1, but unstable in Cases 2 and 3. These results indicate that when adjusting parameters according to the rules in the previous section, the following aspects should be considered: First, the bandwidth of the power decoupling loop should not be too high, which can adversely affect system stability. Second, the current loop bandwidth should not be too low, as this can degrade the dynamic performance and violate the time-scale separation principle, potentially leading to system instability. Moreover, an overly high current loop bandwidth is also undesirable, as it may amplify noise and induce high-frequency oscillations.

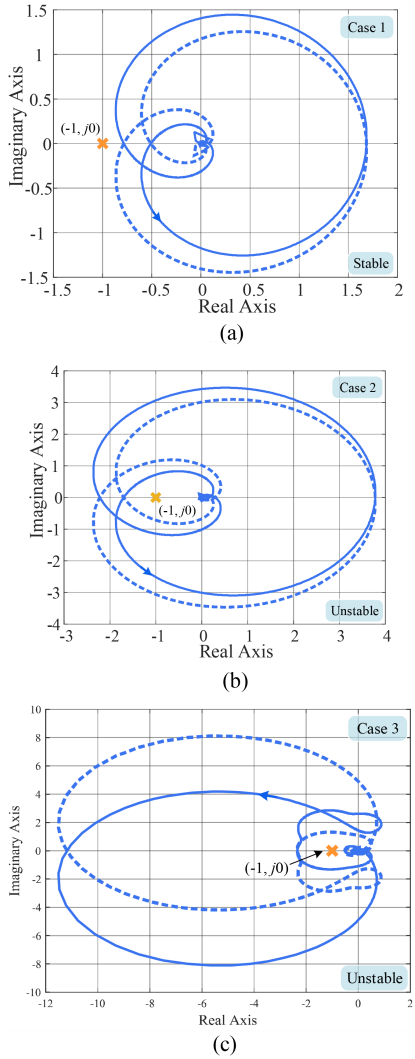

Fig. 6. Nyquist diagram of $\det\{-\boldsymbol{Z}_o\boldsymbol{Y}\}$ in cases 1–3. (a) Case 1. (b) Case 2. (c) Case 3.

IV. EXPERIMENTAL VALIDATION

An experimental prototype of the single-phase DCI is developed to verify the effectiveness of the proposed control method. Fig. 7 shows the hardware prototype of the DCI and the system parameters are provided in Table II. A TMS320F28335 floating-point digital signal processor is used to implement the proposed control strategy and generate the required PWM signals for the DCI. The input voltage is supplied by a programmable dc power supply.

A. Power Decoupling Performance Verification

To validate the effectiveness of the proposed power decoupling control strategy, comparative experiments are conducted with and without power decoupling. The experimental results are presented in Fig. 8. As shown in Fig. 8(a), disabling power decoupling control results in a significant second-order ripple in the input current. Consequently, the presence of the second

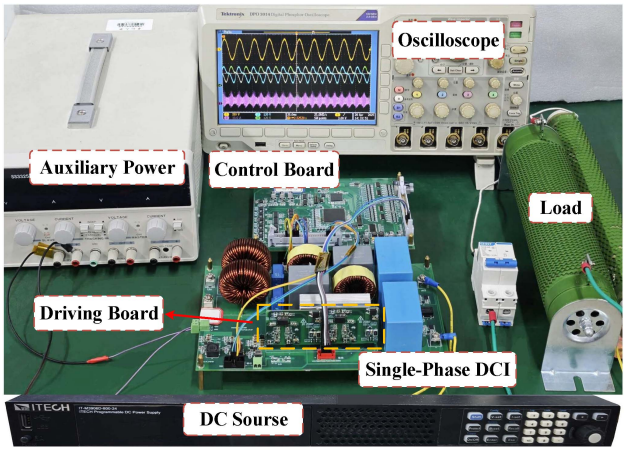

Fig. 7. Experimental prototype of the single-phase DCI.

TABLE II
MAIN CIRCUIT AND CONTROLLER PARAMETERS

Symbol	Descriptions	Value
P_o	Rated output power	480 W
u_o	Output voltage	110 V(rms)
ω_1	Output angular frequency	100 π rad/s
E	Input voltage	150 V
L_1	Input inductor	1 mH
C_1	Blocking capacitor	20 μF
L_2	Output inductor	0.9 mH
C_2	Output capacitor	40 μF
f_s	Switching frequency	20 kHz
k_{pr1}, k_{r1}	PR_1 controller gains	0.075, 30
k_{pr2}, k_{r2}	PR_2 controller gains	13, 50
ξ_1, ξ_2	Damping ratio of Notch filter	0.09, 0.05
k_{p1}, k_{i1}	PI_1 controller gains	0.07, 5
k_{p2}, k_{i2}	PI_2 controller gains	13, 50
$k_{r1\text{-}3}$	Resonant controller R_1 gains	10
$k_{r2\text{-}3}$	Resonant controller R_2 gains	20
$k_{r3\text{-}2}$, $k_{r3\text{-}4}$	Resonant controller R_3 gains	50, 20
$u^*_{\Sigma 2(0)}$	Reference to the dc component of $u_{\Sigma 2}$	280 V

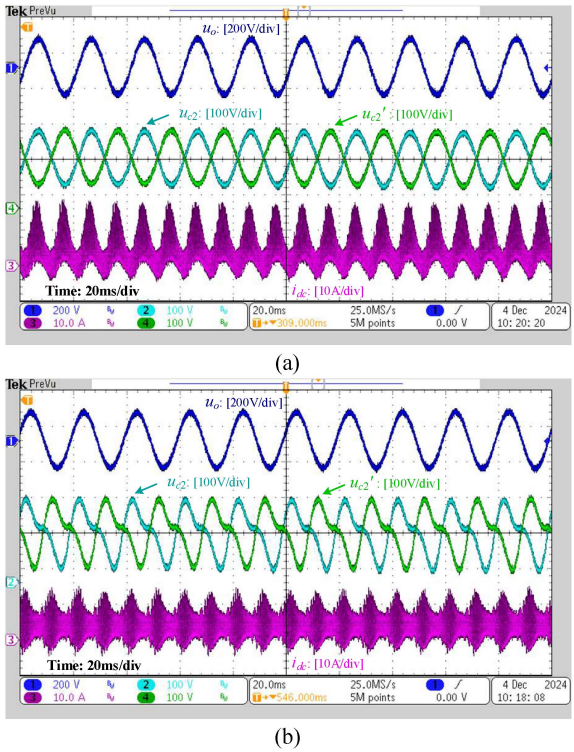

Fig. 8. Comparative experimental results. (a) Without the proposed power decoupling control. (b) With power decoupling control.

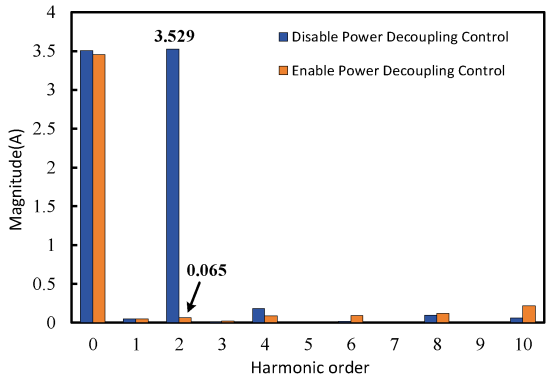

Fig. 9. Spectrum of input current $i_{\Sigma 1}$ when disabling/enabling proposed power decoupling control method.

harmonic component increases the current stress on the power switches.

Fig. 8(b) shows the steady-state waveforms of DCI under the proposed power decoupling control method. The THD values of the output voltage with and without power decoupling are 2.86% and 3.21%, respectively. As observed, the difference in output voltage harmonics under the two conditions is relatively small. These results demonstrate that the proposed APD control strategy achieves power decoupling without compromising the quality of the output voltage.

Additionally, it is observed that the double-line-frequency component of the input current $i_{\Sigma 1}$ is effectively suppressed by the power decoupling control. Fig. 9 illustrates the spectrum of input current $i_{\Sigma 1}$ before and after the power decoupling control is enabled. It is noted that the second harmonic component of the input current is effectively reduced from 3.529 A to 0.078 A, which represents a reduction of 97.8%. These experimental results indicate that the proposed control strategy exhibits excellent power decoupling performance.

The experimental results of transient waveforms when enabling power decoupling control are shown in Fig. 10. After applying the power decoupling control method, the second-order pulsating component in the input current is rapidly and effectively reduced.

Furthermore, the average value of $u_{\Sigma 2}$ is controlled to 280 V, both with and without power decoupling, as shown in Fig. 10(b). The experimental results demonstrate that the actual value is consistent with the reference value, indicating that the proposed control strategy effectively controls the average value of the sum of capacitor voltages.

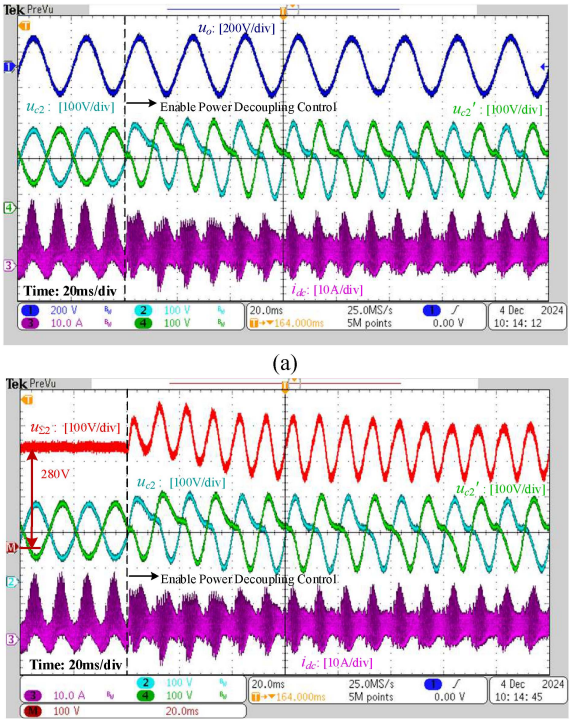

Fig. 10. Experimental results of transient waveforms for enabling power decoupling control. (a) u_o, u_{c2}, u'_{c2}, and i_{dc}. (b) $u_{\Sigma 2}, uc2, u'_{c2}$, and i_{dc}.

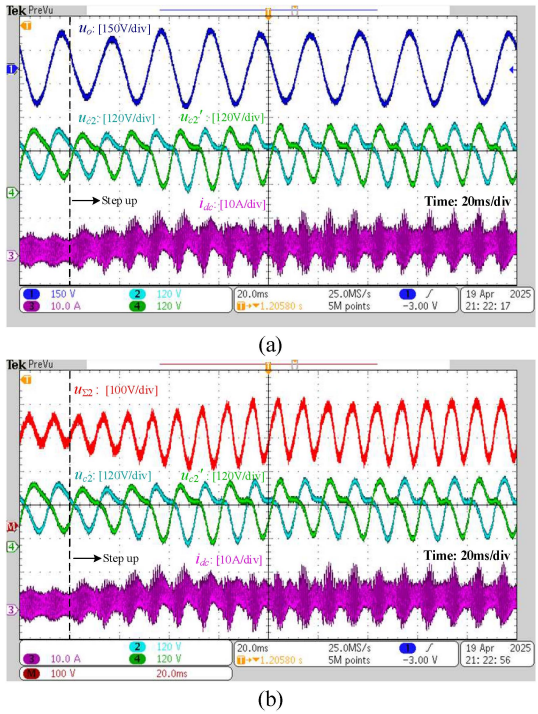

Fig. 11. Dynamic experimental results with a step-up change in the load 240 W–480 W. (a) u_o, u_{c2}, u'_{c2}, and i_{dc}. (b) $u_{\Sigma 2}, u_{c2}, u'_{c2}$, and i_{dc}.

In addition, a 100 Hz component is clearly discernible in the output side capacitor voltage, suggesting that the pulsating power is automatically absorbed by the capacitors without propagating to the dc side. The experimental results confirm the correctness of the proposed APD control strategy.

B. Dynamic Experimental Results

Fig. 11 presents the dynamic experimental results under the rated output voltage condition, where the load increases from half-load (240 W) to full-load (480 W). As observed, the input current $i_{\Sigma 1}$ quickly tracks the reference. Additionally, an increase in the amplitude of the 100 Hz component is observed in the capacitor voltage. This is evident in Fig. 11(b), where an obvious fluctuation of $u_{\Sigma 2}$ is noticeable.

As illustrated in Fig. 12, the load changes from full-load to half-load, the stabilization time is 0.1 s. Throughout the dynamic transient, no significant overcurrent is observed. The results demonstrate that the proposed APD control method exhibits good dynamic performance.

C. Stability Validation

Experiments under different cases are conducted to validate the effectiveness of stability analysis and the results are shown in Fig. 13. Initially, the system operates under Case 1. The output voltage is a sinusoidal wave and no oscillation occurs in the dc current, which indicates that the system is stable. Subsequently, the parameters of the power decoupling controller PI_1 are changed from Case 1 to Case 2. As illustrated in Fig. 13(a), a significant distortion emerges in the voltage, while the input current gradually diverges, which clearly demonstrates that the system becomes unstable.

Similarly, as shown in Fig. 13(b), when the parameters of the input current controller PI_2 are modified from Case 1 to Case 3, the input current appears obvious oscillations and starts to diverge, which implies the system is unstable. Overall, the experimental results are in excellent agreement with the analytical outcomes presented in Fig. 6, thus confirming the correctness of the stability analysis.

TABLE III
COMPARISON OF THE SWITCH STRESS IN DCI WITH AND WITHOUT POWER DECOUPLING CONTROL UNDER $P_o = 480$ W, $E = 150$ V

State	Without Power Decoupling	With Power Decoupling
Voltage Stress	2.39 p.u.	2.50 p.u.
Current Stress	3.62 p.u.	3.13 p.u.

D. Stress Analysis of Power Device

Based on the steady-state analysis, the calculated device stress values with and without power decoupling are summarized in Table III [15]. The benchmark values are chosen as: $U_o = 1.0$ p.u., $I_o = 1.0$ p.u. with full load $P_o = 480$ W, and the dc-link voltage $E = 150$ V.

As observed, the implementation of the proposed power decoupling control strategy results in a slight increase in the voltage stress of switching devices. However, it yields an approximate 13.5% reduction in current stress.

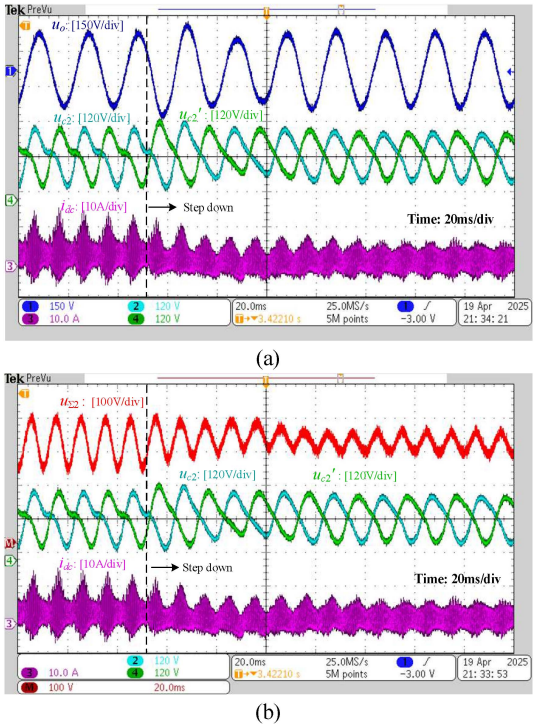

Fig. 12. Dynamic experimental results with a step-down change in the load 480 W–240 W. (a) u_o, u_{c2}, u'_{c2}, and i_{dc}. (b) $u\Sigma 2, u_{c2}, u'_{c2}$, and i_{dc}.

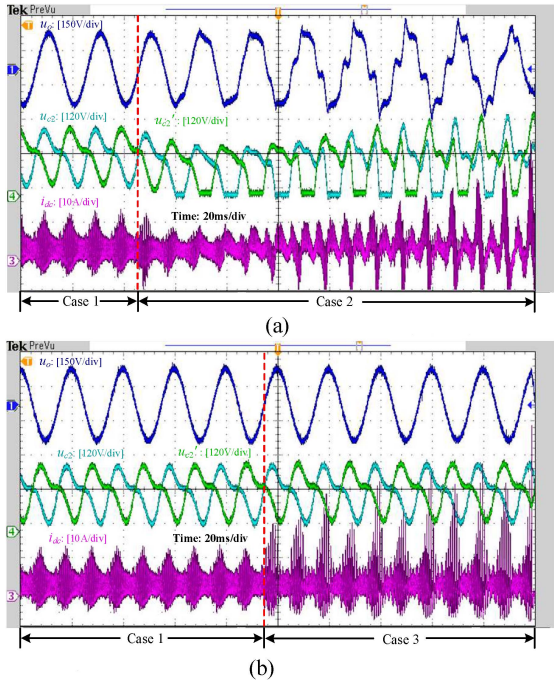

Fig. 13. Experimental results under different cases. (a) Experimental waveforms from Case 1 to Case 2. (b) Experimental waveforms from Case 1 to Case 3.

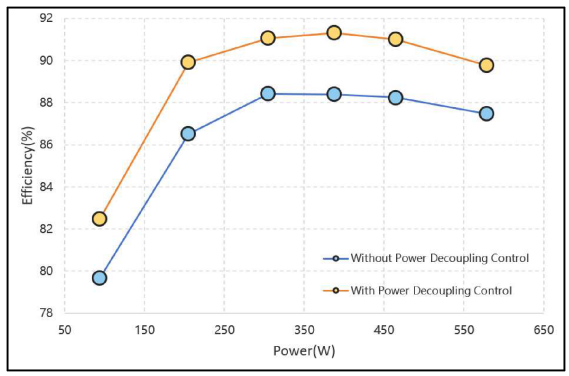

Fig. 14. Measured efficiency curves of single-phase DCI system.

E. Efficiency Analysis

The efficiency of the experimental setup is measured using a power analyzer (PA5000H). Fig. 14 shows the measured efficiency curves with and without power decoupling control at various output power levels. The maximum efficiency observed over the tested power range is 91.29%. Furthermore, it is evident that enabling the proposed APD control results in a significant improvement in system efficiency.

The breakdown of the theoretically calculated system losses at rated power, with and without power decoupling, is shown in Fig. 15 [38], [39], [40]. As seen, both the conduction loss and switching loss of the switching device are reduced after power decoupling. And the decrease in conduction loss is the main reason for the efficiency improvement. Moreover, based on the previous analysis of switching stress in DCI, the proposed power decoupling control strategy reduces the current stress on switching devices, which is an important contributing factor to the improvement of system efficiency.

F. Performance Comparison of Power Decoupling-Based Differential Inverters

Table IV presents a performance comparison between the proposed control strategy and several existing power decoupling-based differential inverters. The differential buck inverter in [29] exhibits comparable efficiency and power density to the DCI presented in this manuscript. However, its controller design process is significantly complex. The differential buck–boost inverter in [25], designed using an ANN-based multiple-objective optimization approach, shows higher efficiency and power density than other differential inverters. Nevertheless, this topology requires eight switches and operates at a higher switching frequency, resulting in a high cost. In [9], the differential buck–boost inverter adopts an open-loop ripple calculation method, resulting in relatively weak power decoupling performance.

The abovementioned methods all adopt DPD control. In contrast, the differential boost inverter in [28] employs a virtual impedance control strategy to directly suppresses the low-frequency harmonics in the input current, which is regarded as an APD control. Notably, due to the direct regulation of input current, both the APD method in [28] and the proposed APD method achieve a higher suppression rate of second-order ripple than those DPD methods. Furthermore, the proposed APD strategy for DCI improves overall system efficiency and maintains high-quality output voltage. However, the proposed

TABLE IV
PERFORMANCE COMPARISON OF POWER DECOUPLING-BASED DIFFERENTIAL INVERTERS

Topology		Differential buck inverter	Differential boost inverter	Eight-switch Differential buck–boost inverter	Differential buck–boost inverter	Differential Cuk inverter
Ref.		[29]	[28]	[25]	[9]	This article
Number of	L, C	3, 3[1)]	2, 2	2, 2	2, 2	4, 4
	S	4	4	8	4	4
Switching frequency f_s		-	20 kHz	50 kHz	12 kHz	20 kHz
Type of power decoupling		DPD	APD	DPD	DPD	APD
Control Strategy Complexity		Complex	Complex	Moderate	Simple	Moderate
Second-order ripple suppression ratio [2)]		95.3%	96.6%	90.6%	>50%	97.8%
Maximum efficiency		91.39%	≈94%	97.78%	≈88%	91.29%
Efficiency variation [3)]		-	≈+2.6%	-	≈+1%	≈+2.9%
Minimum THD [4)]		3.47%	-	-	5.9%	2.86%
Rated power		660 W	250 W	1.8 kW	400 W	480 W
Power density		Middle	Middle	High	Middle	Middle
Cost		Middle	Middle	High	Middle	High

1) An input-side LC filter to ensure continuous input current. 2) Suppression ratio of second-order ripple in the input current. 3) Efficiency variation before and after power decoupling, under rated power. 4) Measured under power decoupling control.

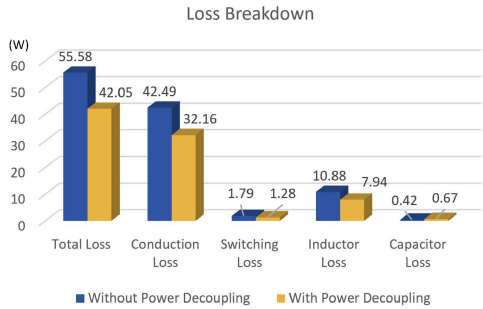

Fig. 15. Comparison of the theoretically calculated loss breakdown at rated power, with and without the proposed power decoupling control method.

control strategy is relatively complex. Therefore, it provides an effective tradeoff between performance and practical feasibility.

V. CONCLUSION

This article proposes a new control strategy for single-phase DCI. The control scheme is based on the models of DCI in both common-mode and differential-mode. Compared with the existing methods, it not only realizes excellent power decoupling performance but also improves the efficiency up to about 3%. In addition, parameter selection rules for the proposed power decoupling control strategy are presented to guide practical implementation. As the DCI with power decoupling is a nonlinear time-periodic system, a small-signal stability analysis considering frequency coupling is carried out. The detailed procedures for impedance modeling and corresponding stability analysis criteria are provided. Experimental results validate the effectiveness of the proposed control scheme and confirm the accuracy of the stability analysis. This study focuses exclusively on the control of the DCI under OFF-grid operation. The grid-connected operation, as another common application field, deserves further study.

APPENDIX

A. Circuit Modeling

According to the steady-state analysis in Section II, it is reasonably assumed that the steady-state trajectory of the system is

$$\begin{cases} \bar{d}_1(t) = D_{1,0} + D_{1,1}\cos(\omega_1 t + \varphi_{d1,1}) \\ \quad + D_{1,2}\cos(2\omega_1 t + \varphi_{d1,2}) + D_{1,3}\cos(3\omega_1 t + \varphi_{d1,3}) \\ \bar{u}_{c1}(t) = U_{1,0} + U_{1,1}\cos(\omega_1 t + \varphi_{u1,1}) \\ \quad + U_{1,2}\cos(2\omega_1 t + \varphi_{u1,2}) \\ \bar{u}_{c2}(t) = U_{2,0} + U_{2,1}\cos(\omega_1 t + \varphi_{u2,1}) \\ \quad + U_{2,2}\cos(2\omega_1 t + \varphi_{u2,2}) \\ \bar{i}_{L1}(t) = I_{1,0} + I_{1,1}\cos(\omega_1 t + \varphi_{i1,1}) \\ \quad + I_{1,3}\cos(3\omega_1 t + \varphi_{i1,3}) \\ \bar{i}_{L2}(t) = I_{2,1}\cos(\omega_1 t + \varphi_{i2,1}) + I_{2,2}\cos(2\omega_1 t + \varphi_{i2,2}) \end{cases} \tag{A1}$$

where X_a denotes the state variables and duty cycles. $X_{a,0}$ represents the dc component of X_a while $X_{a,1}$ and $\varphi_{xa,1}$ represent the amplitude and phase angle of the 50 Hz sinusoidal component, respectively. The remaining symbols denote the amplitudes and phase angles of the second and third harmonics. And the trajectories of module 2 are similar to (A1). The above approximate results retain only up to the third harmonic component, while higher order harmonics are neglected. This simplification is reasonable, as the amplitudes of higher-frequency components are small.

Taking the model of Cuk module 1 as an example, and module 2 is similar to it. According to (1), the small-signal model of Cuk

module 1 is expressed as

$$\begin{cases} L_1\frac{d\tilde{i}_{L1}(t)}{dt} = -\tilde{u}_{c1}(t) + \bar{d}_1(t)\,\tilde{u}_{c1}(t) + \bar{u}_{c1}(t)\,\tilde{d}_1(t) \\ C_1\frac{d\tilde{u}_{c1}(t)}{dt} = -\bar{d}_1(t)\,\tilde{i}_{L2}(t) - \bar{i}_{L2}(t)\,\tilde{d}_1(t) + \tilde{i}_{L1}(t) \\ \qquad\qquad -\bar{d}_1(t)\,\tilde{i}_{L1}(t) - \bar{i}_{L1}(t)\,\tilde{d}_1(t) \\ L_1\frac{d\tilde{i}_{L2}(t)}{dt} = \bar{d}_1(t)\,\tilde{u}_{c1}(t) + \bar{u}_{c1}(t)\,\tilde{d}_1(t) - \tilde{u}_{c2}(t) \\ C_2\frac{d\tilde{u}_{c2}(t)}{dt} = \tilde{i}_{L2}(t) - \tilde{i}_o(t) \end{cases} \tag{A2}$$

where the superscript "-" represents the steady-state trajectory, and "$\sim$" represents the small-signal quantity. Substituting the steady-state trajectories (A1) into (A2) and transforming it to the frequency domain, then taking frequency-shifting and frequency truncation operations yields

$$\begin{cases} \boldsymbol{G}_{iL1}\tilde{\boldsymbol{i}}_{L1} = \boldsymbol{G}_{iL1\_uc1}\tilde{\boldsymbol{u}}_{c1} + \boldsymbol{G}_{iL1\_d1}\tilde{\boldsymbol{d}}_1 \\ \boldsymbol{G}_{uc1}\tilde{\boldsymbol{u}}_{c1} = \boldsymbol{G}_{uc1\_iL2}\tilde{\boldsymbol{i}}_{L2} + \boldsymbol{G}_{uc1\_iL1}\tilde{\boldsymbol{i}}_{L1} + \boldsymbol{G}_{iL12\_d1}\tilde{\boldsymbol{d}}_1 \\ \boldsymbol{G}_{iL2}\tilde{\boldsymbol{i}}_{L2} = \boldsymbol{G}_{iL2\_uc1}\tilde{\boldsymbol{u}}_{c1} + \boldsymbol{G}_{iL2\_d1}\tilde{\boldsymbol{d}}_1 + \boldsymbol{G}_{iL2\_uc2}\tilde{\boldsymbol{u}}_{c2} \\ \boldsymbol{G}_{uc2}\tilde{\boldsymbol{u}}_{c2} = \boldsymbol{G}_{uc2\_iL2}\tilde{\boldsymbol{i}}_{L2} + \boldsymbol{G}_{uc2\_io}\tilde{\boldsymbol{i}}_o \end{cases} \tag{A3}$$

where $\tilde{\boldsymbol{x}}$= [$\tilde{x}(s + j3\omega_1)$ $\tilde{x}(s + j2\omega_1)$ $\tilde{x}(s + j\omega_1)$ $\tilde{x}(s)$ $\tilde{x}(s$ - $j\omega_1)$ $\tilde{x}(s$ - $j\omega_1)$ $\tilde{x}(s - j2\omega_1)$ $\tilde{x}(s - j3\omega_1)]^T$ represents the state variables and the duty cycles. Taking matrix $\boldsymbol{G}_{iL1}$ and $\boldsymbol{G}_{iL1\_uc1}$ as examples, the remaining coefficient matrices have the forms that are represented in (A4) and (A5):

$$\boldsymbol{G}_{iL1} = diag \begin{bmatrix} G_{iL1}(s + j3\omega_1) & \cdots & G_{iL1}(s) & \cdots & G_{iL1}(s - j3\omega_1) \end{bmatrix} \tag{A4}$$

where *diag*[] represents the diagonal matrix or block diagonal matrix. And (A5) is shown at the bottom of this page, where $G_{iL1}(s) = L_1 s$, $G^3_{iL1\_uc1}(s) = \frac{D_{1,3}e^{-j\varphi_{d1,3}}}{2}$, $G^2_{iL1\_uc1}(s) = \frac{D_{1,2}e^{-j\varphi_{d1,2}}}{2}$, $G^1_{iL1\_uc1}(s) = \frac{D_{1,1}e^{-j\varphi_{d1,1}}}{2}$, $G^0_{iL1\_uc1}(s) = D_{1,0} - 1$, $G^{-1}_{iL1\_uc1}(s) = \frac{D_{1,1}e^{j\varphi_{d1,1}}}{2}$, $G^{-2}_{iL1\_uc1}(s) = \frac{D_{1,2}e^{j\varphi_{d1,2}}}{2}$, $G^{-3}_{iL1\_uc1}(s) = \frac{D_{1,3}e^{j\varphi_{d1,3}}}{2}$. The remaining terms of (A5) can be obtained by frequency-shifting

Similarly, the matrix model of module 2 is obtained as follows:

$$\begin{cases} \boldsymbol{G}_{i'L1}\tilde{\boldsymbol{i}}'_{L1} = \boldsymbol{G}_{i'L1\_u'c1}\tilde{\boldsymbol{u}}'_{c1} + \boldsymbol{G}_{i'L1\_d2}\tilde{\boldsymbol{d}}_2 \\ \boldsymbol{G}_{u'c1}\tilde{\boldsymbol{u}}'_{c1} = \boldsymbol{G}_{u'c1\_i'L2}\tilde{\boldsymbol{i}}'_{L2} + \boldsymbol{G}_{u'c1\_i'L1}\tilde{\boldsymbol{i}}'_{L1} + \boldsymbol{G}_{i'L12\_d2}\tilde{\boldsymbol{d}}_2 \\ \boldsymbol{G}_{i'L2}\tilde{\boldsymbol{i}}'_{L2} = \boldsymbol{G}_{i'L2\_u'c1}\tilde{\boldsymbol{u}}'_{c1} + \boldsymbol{G}_{i'L2\_d2}\tilde{\boldsymbol{d}}_2 + \boldsymbol{G}_{i'L2\_u'c2}\tilde{\boldsymbol{u}}'_{c2} \\ \boldsymbol{G}_{u'c2}\tilde{\boldsymbol{u}}'_{c2} = \boldsymbol{G}_{u'c2\_i'L2}\tilde{\boldsymbol{i}}'_{L2} + \boldsymbol{G}_{u'c2\_io}\tilde{\boldsymbol{i}}_o \end{cases} \tag{A6}$$

B. Control Loop Modeling

According to the model of the output voltage control loop (22)–(26), by performing the aforementioned linearization and frequency-shifting operations, the following matrix models are obtained:

$$\tilde{\boldsymbol{\mu}}_1 = \boldsymbol{G}_{\mu1\_u\Delta2}\tilde{\boldsymbol{u}}_{\Delta2} \tag{B1}$$

$$\boldsymbol{G}_{\lambda}\tilde{\boldsymbol{\lambda}} = \boldsymbol{G}_{\lambda\_u\Sigma1}\tilde{\boldsymbol{u}}_{\Sigma1} + \boldsymbol{G}_{\lambda\_u\Delta1}\tilde{\boldsymbol{u}}_{\Delta1} \tag{B2}$$

$$\boldsymbol{G}_{i*\Delta1}\tilde{\boldsymbol{i}}^*_{\Delta1} = \boldsymbol{G}_{i*\Delta1\_\lambda}\tilde{\boldsymbol{\lambda}} + \boldsymbol{G}_{i*\Delta1\_\mu1}\tilde{\boldsymbol{\mu}}_1 \tag{B3}$$

Similarly, based on (27)–(29), the matrix model of the power decoupling control loop is expressed as

$$\tilde{\boldsymbol{i}}^*_{\Sigma1} = \boldsymbol{G}_{i*\Sigma1\_u\Sigma2}\tilde{\boldsymbol{u}}_{\Sigma2} \tag{B4}$$

Moreover, the matrix models for the current control loop (30)–(34) are shown as

$$\begin{cases} \tilde{\boldsymbol{\nu}}_1 = \boldsymbol{G}_{v1\_i\Delta1}\tilde{\boldsymbol{i}}^*_{\Delta1} - \boldsymbol{G}_{v1\_i\Delta1}\tilde{\boldsymbol{i}}_{\Delta1} \\ \tilde{\boldsymbol{\nu}}_2 = \boldsymbol{G}_{v2\_i\Sigma1}\tilde{\boldsymbol{i}}^*_{\Sigma1} - \boldsymbol{G}_{v2\_i\Sigma1}\tilde{\boldsymbol{i}}_{\Sigma1} \end{cases} \tag{B5}$$

$$\begin{cases} \boldsymbol{G}_{d1}\tilde{\boldsymbol{d}}_1 = \tilde{\boldsymbol{\nu}}_1 + \tilde{\boldsymbol{\nu}}_2 + \boldsymbol{G}_{d1\_u\Delta1}\tilde{\boldsymbol{u}}_{\Delta1} + \boldsymbol{G}_{d1\_u\Sigma1}\tilde{\boldsymbol{u}}_{\Sigma1} \\ \boldsymbol{G}_{d2}\tilde{\boldsymbol{d}}_2 = \tilde{\boldsymbol{\nu}}_1 - \tilde{\boldsymbol{\nu}}_2 + \boldsymbol{G}_{d2\_u\Delta1}\tilde{\boldsymbol{u}}_{\Delta1} + \boldsymbol{G}_{d2\_u\Sigma1}\tilde{\boldsymbol{u}}_{\Sigma1} \end{cases} \tag{B6}$$

$$\boldsymbol{G}_{iL1\_uc1} = \begin{bmatrix} G^0_{iL1\_uc1}(s + j3\omega_1) & G^{-1}_{iL1\_uc1}(s + j3\omega_1) & G^{-2}_{iL1\_uc1}(s + j3\omega_1) & G^{-3}_{iL1\_uc1}(s + j3\omega_1) \\ G^1_{iL1\_uc1}(s + j2\omega_1) & G^0_{iL1\_uc1}(s + j2\omega_1) & G^{-1}_{iL1\_uc1}(s + j2\omega_1) & G^{-2}_{iL1\_uc1}(s + j2\omega_1) \\ G^2_{iL1\_uc1}(s + j\omega_1) & G^1_{iL1\_uc1}(s + j\omega_1) & G^0_{iL1\_uc1}(s + j\omega_1) & G^{-1}_{iL1\_uc1}(s + j\omega_1) \\ G^3_{iL1\_uc1}(s) & G^2_{iL1\_uc1}(s) & G^1_{iL1\_uc1}(s) & G^0_{iL1\_uc1}(s) \\ 0 & G^3_{iL1\_uc1}(s - j\omega_1) & G^2_{iL1\_uc1}(s - j\omega_1) & G^1_{iL1\_uc1}(s - j\omega_1) \\ 0 & 0 & G^3_{iL1\_uc1}(s - j2\omega_1) & G^2_{iL1\_uc1}(s - j2\omega_1) \\ 0 & 0 & 0 & G^3_{iL1\_uc1}(s - j3\omega_1) \end{bmatrix}$$

$$\begin{bmatrix} 0 & 0 & 0 \\ G^{-3}_{iL1\_uc1}(s + j2\omega_1) & 0 & 0 \\ G^{-2}_{iL1\_uc1}(s + j\omega_1) & G^{-3}_{iL1\_uc1}(s + j\omega_1) & 0 \\ G^{-1}_{iL1\_uc1}(s) & G^{-2}_{iL1\_uc1}(s) & G^{-3}_{iL1\_uc1}(s) \\ G^0_{iL1\_uc1}(s - j\omega_1) & G^{-1}_{iL1\_uc1}(s - j\omega_1) & G^{-2}_{iL1\_uc1}(s - j\omega_1) \\ G^1_{iL1\_uc1}(s - j2\omega_1) & G^0_{iL1\_uc1}(s - j2\omega_1) & G^{-1}_{iL1\_uc1}(s - j2\omega_1) \\ G^2_{iL1\_uc1}(s - j3\omega_1) & G^1_{iL1\_uc1}(s - j3\omega_1) & G^0_{iL1\_uc1}(s - j3\omega_1) \end{bmatrix} \tag{A5}$$

$$\mathbf{B}=\begin{bmatrix}
\mathbf{0} & \boldsymbol{G}_{iL1_uc1} & \mathbf{0} & \mathbf{0} & \boldsymbol{G}_{iL1_d1} & \mathbf{0} & \mathbf{0} & \mathbf{0} & \mathbf{0} & \mathbf{0}\\
\boldsymbol{G}_{uc1_iL1} & \mathbf{0} & \boldsymbol{G}_{uc1_iL2} & \mathbf{0} & \boldsymbol{G}_{uc1_d1} & \mathbf{0} & \mathbf{0} & \mathbf{0} & \mathbf{0} & \mathbf{0}\\
\mathbf{0} & \boldsymbol{G}_{iL2_uc1} & \mathbf{0} & \boldsymbol{G}_{iL2_uc2} & \boldsymbol{G}_{iL2_d1} & \mathbf{0} & \mathbf{0} & \mathbf{0} & \mathbf{0} & \mathbf{0}\\
\mathbf{0} & \mathbf{0} & \boldsymbol{G}_{uc2_iL2} & \mathbf{0} & \mathbf{0} & \mathbf{0} & \mathbf{0} & \mathbf{0} & \mathbf{0} & \mathbf{0}\\
\boldsymbol{G}_{d1iL1} & \boldsymbol{G}_{d1uc1} & \mathbf{0} & \boldsymbol{G}_{d1uc2} & \mathbf{0} & \boldsymbol{G}_{d1i'L1} & \boldsymbol{G}_{d1u'c1} & \mathbf{0} & \boldsymbol{G}_{d1u'c2} & \mathbf{0}\\
\mathbf{0} & \mathbf{0} & \mathbf{0} & \mathbf{0} & \mathbf{0} & \mathbf{0} & \boldsymbol{G}_{i'L1_u'c1} & \mathbf{0} & \mathbf{0} & \boldsymbol{G}_{i'L1_d2}\\
\mathbf{0} & \mathbf{0} & \mathbf{0} & \mathbf{0} & \mathbf{0} & \boldsymbol{G}_{u'c1_i'L1} & \mathbf{0} & \boldsymbol{G}_{u'c1_i'L2} & \mathbf{0} & \boldsymbol{G}_{u'c1_d2}\\
\mathbf{0} & \mathbf{0} & \mathbf{0} & \mathbf{0} & \mathbf{0} & \mathbf{0} & \boldsymbol{G}_{i'L2_u'c1} & \mathbf{0} & \boldsymbol{G}_{i'L2_u'c2} & \boldsymbol{G}_{i'L2_d2}\\
\mathbf{0} & \mathbf{0} & \mathbf{0} & \mathbf{0} & \mathbf{0} & \mathbf{0} & \mathbf{0} & \boldsymbol{G}_{u'c2_i'L2} & \mathbf{0} & \mathbf{0}\\
\boldsymbol{G}_{d2iL1} & \boldsymbol{G}_{d2uc1} & \mathbf{0} & \boldsymbol{G}_{d2u'c2} & \mathbf{0} & \boldsymbol{G}_{d2i'L1} & \boldsymbol{G}_{d2u'c1} & \mathbf{0} & \boldsymbol{G}_{d2u'c2} & \mathbf{0}
\end{bmatrix} \tag{C6}$$

C. Impedance Modeling

Combining (B1)–(B6), the relationships between the duty cycles and state variables in the control loops are given as

$$\begin{aligned}\tilde{\boldsymbol{d}}_1 &= \boldsymbol{G}_{d1uc1}\tilde{\boldsymbol{u}}_{c1}+\boldsymbol{G}_{d1u'c1}\tilde{\boldsymbol{u}}'_{c1}+\boldsymbol{G}_{d1uc2}\tilde{\boldsymbol{u}}_{c2}\\ &\quad+\boldsymbol{G}_{d1u'c2}\tilde{\boldsymbol{u}}'_{c2}+\boldsymbol{G}_{d1iL1}\tilde{\boldsymbol{i}}_{L1}+\boldsymbol{G}_{d1i'L1}\tilde{\boldsymbol{i}}'_{L1}\end{aligned} \tag{C1}$$

$$\begin{aligned}\tilde{\boldsymbol{d}}_2 &= \boldsymbol{G}_{d2uc1}\tilde{\boldsymbol{u}}_{c1}+\boldsymbol{G}_{d2u'c1}\tilde{\boldsymbol{u}}'_{c1}+\boldsymbol{G}_{d2uc2}\tilde{\boldsymbol{u}}_{c2}\\ &\quad+\boldsymbol{G}_{d2u'c2}\tilde{\boldsymbol{u}}'_{c2}+\boldsymbol{G}_{d2iL1}\tilde{\boldsymbol{i}}_{L1}+\boldsymbol{G}_{d2i'L1}\tilde{\boldsymbol{i}}'_{L1}\end{aligned} \tag{C2}$$

Rewriting (A3), (A6), and (C2) in the form of a large matrix yields

$$\mathbf{AX}=\mathbf{BX}+\mathbf{C}\tilde{\boldsymbol{i}}_o \tag{C3}$$

where $\mathbf{X}=[\tilde{\boldsymbol{i}}_{L1}\ \tilde{\boldsymbol{u}}_{c1}\ \tilde{\boldsymbol{i}}_{L2}\ \tilde{\boldsymbol{u}}_{c2}\ \tilde{\boldsymbol{d}}_1\ \tilde{\boldsymbol{i}}'_{L1}\ \tilde{\boldsymbol{u}}'_{c1}\ \tilde{\boldsymbol{i}}'_{L2}\ \tilde{\boldsymbol{u}}'_{c2}\ \tilde{\boldsymbol{d}}_2]^T$. Matrices $\mathbf{A}$ and $\mathbf{C}$ are given in (C4) and (C5), respectively. $\mathbf{B}$ is given in (C6), as shown at the top of this page

$$\mathbf{A}=diag\left[\boldsymbol{G}_{iL1}\ \boldsymbol{G}_{uc1}\ \boldsymbol{G}_{iL2}\ \boldsymbol{G}_{uc2}\ \boldsymbol{I}\ \boldsymbol{G}_{i'L1}\ \boldsymbol{G}_{u'c1}\ \boldsymbol{G}_{i'L2}\ \boldsymbol{G}_{u'c2}\ \boldsymbol{I}\right] \tag{C4}$$

$$\mathbf{C}=\begin{bmatrix}\mathbf{0} & \mathbf{0} & \mathbf{0} & \boldsymbol{G}_{uc2\_io} & \mathbf{0} & \mathbf{0} & \mathbf{0} & \mathbf{0} & \boldsymbol{G}_{u'c2\_io} & \mathbf{0}\end{bmatrix}^T \tag{C5}$$

where $\boldsymbol{I}$ represents a 7×7 identity matrix and $\mathbf{0}$ represents a 7×7 zero matrix.

Furthermore, the output equation of DCI is expressed as

$$\tilde{\boldsymbol{u}}_o=\mathbf{DX} \tag{C7}$$

where $\tilde{\boldsymbol{u}}_o=\tilde{\boldsymbol{u}}_{c2}-\tilde{\boldsymbol{u}}'_{c2}$, and matrix $\mathbf{D}$ is given as

$$\mathbf{D}=\begin{bmatrix}\mathbf{0} & \mathbf{0} & \mathbf{0} & \boldsymbol{I} & \mathbf{0} & \mathbf{0} & \mathbf{0} & \mathbf{0} & -\boldsymbol{I} & \mathbf{0}\end{bmatrix} \tag{C8}$$

Substituting (C3) into (C7) yields

$$\tilde{\boldsymbol{u}}_o=\mathbf{D}(\mathbf{A}-\mathbf{B})^{-1}\mathbf{C}\tilde{\boldsymbol{i}}_o \tag{C9}$$

Therefore, the output impedance of DCI with power decoupling is obtained

$$\boldsymbol{Z}_o=\mathbf{D}(\mathbf{A}-\mathbf{B})^{-1}\mathbf{C} \tag{C10}$$

REFERENCES

[1] A. Ch. Kyritsis, E. C. Tatakis, and N. P. Papanikolaou, "Optimum design of the current-source flyback inverter for decentralized grid-connected photovoltaic systems," *IEEE Trans. Energy Convers.*, vol. 23, no. 1, pp. 281–293, Mar. 2008.

[2] C. Liu and J.-S. Lai, "Low frequency current ripple reduction technique with active control in a fuel cell power system with inverter load," *IEEE Trans. Power Electron.*, vol. 22, no. 4, pp. 1429–1436, Jul. 2007.

[3] A. A. Khan et al., "Single-stage bidirectional buck–Boost inverters using a Single inductor and eliminating the common-mode leakage current," *IEEE Trans. Power Electron.*, vol. 35, no. 2, pp. 1269–1281, Feb. 2020.

[4] U. A. Khan, A. A. Khan, F. Akbar, and J.-W. Park, "Single-stage Single-phase H6 and H8 non-isolated buck-boost photovoltaic inverters," *IEEE J. Emerg. Sel. Topics Power Electron.*, vol. 10, no. 4, pp. 4865–4878, Aug. 2022.

[5] I. Serban, "Power decoupling method for single-phase H-bridge inverters with No additional Power electronics," *IEEE Trans. Ind. Electron.*, vol. 62, no. 8, pp. 4805–4813, Aug. 2015.

[6] W. Yao, X. Wang, P. C. Loh, X. Zhang, and F. Blaabjerg, "Improved power decoupling scheme for a single-phase grid-connected differential inverter with realistic mismatch in storage capacitances," *IEEE Trans. Power Electron.*, vol. 32, no. 1, pp. 186–199, Jan. 2017.

[7] M. Jang, M. Ciobotaru, and V. G. Agelidis, "A single-phase grid-connected fuel cell system based on a boost-inverter," *IEEE Trans. Power Electron.*, vol. 28, no. 1, pp. 279–288, Jan. 2013.

[8] G.-R. Zhu, S.-C. Tan, and C. K. Tse, "Mitigation of low-frequency current ripple in fuel-cell inverter systems through waveform control," *IEEE Trans. Power Electron.*, vol. 28, no. 2, pp. 779–792, Feb. 2013.

[9] S. Xu, R. Shao, L. Chang, and M. Mao, "Single-phase differential buck–Boost inverter with pulse energy modulation and power decoupling control," *IEEE J. Emerg. Sel. Topics Power Electron.*, vol. 6, no. 4, pp. 2060–2072, Dec. 2018.

[10] W. Yao, Y. Xu, Y. Tang, P. C. Loh, X. Zhang, and F. Blaabjerg, "Generalized power decoupling control for single-phase differential inverters with nonlinear loads," *IEEE J. Emerg. Sel. Topics Power Electron.*, vol. 7, no. 2, pp. 1137–1151, Jun. 2019.

[11] A. Shawky, M. Aly, and J. Rodriguez, "Differential inverters: A general design procedure integrating a novel power losses modeling approach for utilized DC–DC modules at different modulation schemes," *IEEE Access*, vol. 11, pp. 52790–52811, 2023.

[12] S. Mehrnami, "Discontinuous modulation scheme for a differential-mode Ćuk Inverter," *IEEE Trans. Power Electron.*, vol. 30, no. 3, pp. 1242–1254, Mar. 2015.

[13] S. Cuk and R. Erickson, "A conceptually new high-frequency switched-mode amplifier technique eliminates current ripple," in *Proc. 5th Nat. Solid-State Power Conv. Conf.*, May 1978, pp. G3.1–G3.22.

[14] A. Darwish, D. Holliday, S. Ahmed, A. M. Massoud, and B. W. Williams, "A single-stage three-phase inverter based on Cuk converters for PV applications," *IEEE J. Emerg. Sel. Topics Power Electron.*, vol. 2, no. 4, pp. 797–807, Dec. 2014.

[15] K. Tank, S. Gupta, M. M. Garg, S. K. Mazumder, and M. Mohamadi, "A variable-DC-offset modulation scheme for improved performance of a differential-mode inverter," *IEEE Trans. Power Electron.*, vol. 38, no. 12, pp. 15804–15814, Dec. 2023.

[16] S. Mehrnami and H. Soni, "Modulation scheme for three-phase differential-mode Ćuk Inverter," *IEEE Trans. Power Electron.*, vol. 31, no. 3, pp. 2654–2668, Mar. 2016.

[17] H. Soni, S. K. Mazumder, A. Gupta, and A. Kulkarni, "Control of isolated differential-mode single- and three-phase ćuk inverters at module level," *IEEE Trans. Power Electron.*, vol. 33, no. 10, pp. 8872–8886, Oct. 2018.

[18] C. Bao, S. Gupta, and S. K. Mazumder, "Modeling and analysis of peak-current-controlled differential mode Ćuk Inverter," in *Proc. IEEE 12th Int. Symp. Power Electron. Distrib. Gener. Syst.*, Jun. 2021, pp. 1–7.
[19] D. Chatterjee and S. K. Mazumder, "Optimal switching sequence based control of a differential-mode inverter," in *Proc. IEEE 7th Int. Symp. Power Electron. Distrib. Gener. Syst.*, Jun. 2016, pp. 1–8.
[20] Y. Sun, Y. Liu, M. Su, W. Xiong, and J. Yang, "Review of active power decoupling topologies in single-phase systems," *IEEE Trans. Power Electron.*, vol. 31, no. 7, pp. 4778–4794, Jul. 2016.
[21] Y. Liu, W. Zhang, Y. Sun, M. Su, G. Xu, and H. Dan, "Review and comparison of control strategies in active power decoupling," *IEEE Trans. Power Electron.*, vol. 36, no. 12, pp. 14436–14455, Dec. 2021.
[22] B. Chen, Y. Sun, S. Xie, Y. Liu, Y. Lv, and M. Su, "Active power decoupling control for three-level buck four-leg current source inverter," *IEEE Trans. Power Electron.*, vol. 39, no. 12, pp. 15943–15953, Dec. 2024.
[23] Y. Sun, Y. Liu, M. Su, X. Li, and J. Yang, "Active power decoupling method for single-phase current-source rectifier with No additional Active switches," *IEEE Trans. Power Electron.*, vol. 31, no. 8, pp. 5644–5654, Aug. 2016.
[24] R. Musona and I. Serban, "Differential single-phase inverters with active power decoupling: A survey," *IEEE Access*, vol. 11, pp. 53654–53670, 2023.
[25] R. Rajamony, S. Wang, and W. Ming, "Modelling and optimal design of a multifunctional single-stage buck-boost differential inverter," *IEEE Open J. Power Electron.*, vol. 5, pp. 1328–1339, 2024.
[26] S. Li, W. Qi, S.-C. Tan, and S. Y. Hui, "Enhanced automatic-power-decoupling control method for single-phase AC-to-DC converters," *IEEE Trans. Power Electron.*, vol. 33, no. 2, pp. 1816–1828, Feb. 2018.
[27] D. B. W. Abeywardana and V. G. Agelidis, "A rule-based controller to mitigate DC-side second-order harmonic current in a single-phase boost inverter," *IEEE Trans. Power Electron.*, vol. 31, no. 2, pp. 1665–1679, Feb. 2016.
[28] H. Zhou and L. He, "Fractional-order virtual impedance-based low-frequency current ripple mitigation for a differential boost inverter," *IEEE Trans. Ind. Electron.*, vol. 72, no. 6, pp. 5810–5820, Jun. 2025.
[29] H. Li, Y. Sun, Y. Liu, S. Xie, and M. Su, "Coordinate transformation-based nonlinear power decoupling control for differential buck grid-tied inverter," *IEEE Trans. Ind. Electron.*, vol. 70, no. 12, pp. 12201–12210, Dec. 2023.
[30] C. A. Busada, R. A. Fantino, and J. A. Solsona, "High-performance control and power decoupling of a grid-tied differential boost inverter," *IEEE Trans. Power Electron.*, vol. 39, no. 4, pp. 4042–4049, Apr. 2024.
[31] H. Khalil, *Nonlinear Systems*, 3rd ed. New York, NY, USA: Prentice-Hall, 2002.
[32] G. Bengtsson, "Output regulation and internal models—A frequency domain approach," *Automatica*, vol. 13, no. 4, pp. 333–345, Jul. 1977.
[33] N. M. Abdel-Rahim and J. E. Quaicoe, "Analysis and design of a multiple feedback loop control strategy for single-phase voltage-source UPS inverters," *IEEE Trans. Power Electron.*, vol. 11, no. 4, pp. 532–541, Jul. 1996.
[34] J. Lin, M. Su, Y. Sun, D. Yang, and S. Xie, "Recursive SISO impedance modeling of single-phase voltage source rectifiers," *IEEE Trans. Power Electron.*, vol. 37, no. 2, pp. 1296–1309, Feb. 2022.
[35] B. Yu et al., "Frequency-divided control and stability analysis of single-phase three-level flying capacitor boost inverter," *IEEE J. Emerg. Sel. Topics Power Electron.*, vol. 13, no. 1, pp. 1084–1094, Feb. 2025.
[36] Y. Jiang, Y. Sun, J. Lin, W. Xiong, Y. Liu, and M. Su, "Revisit SISO impedance-based stability analysis of single-phase grid-tied converters," *IEEE J. Emerg. Sel. Topics Power Electron.*, vol. 13, no. 1, pp. 637–651, Feb. 2025.
[37] H. Li, Y. Sun, J. Lin, Z. Liu, Y. Liu, and M. Su, "Impedance modeling, measurement and stability analysis of Multi-VSC systems in $\alpha\beta$ coordinate," *IEEE Trans. Sustain. Energy*, vol. 15, no. 4, pp. 2182–2193, Oct. 2024.
[38] M. Z. Farooqi, B. Singh, B. K. Panigrahi, and R. Kumar, "Hybrid modulation and control for multi-objective optimized active power decoupling circuit in AC-to-DC converter," *IEEE Trans. Ind. Appl.*, vol. 61, no. 3, pp. 4054–4064, May/Jun. 2025.
[39] D. Barater, C. Concari, G. Buticchi, E. Gurpinar, D. De, and A. Castellazzi, "Performance evaluation of a three-level ANPC photovoltaic grid-connected inverter with 650-V SiC devices and optimized PWM," *IEEE Trans. Ind. Appl.*, vol. 52, no. 3, pp. 2475–2485, May/Jun. 2016.
[40] S. Lee, F. Chen, T. M. Jahns, and B. Sarlioglu, "PWM for simultaneous minimization of switching losses and CM voltage in current source inverters," *IEEE Trans. Transp. Electrific.*, vol. 10, no. 4, pp. 9788–9802, Dec. 2024.

Yujie Hao was born in Yunnan, China, in 2001. He received the B.S. degree in electrical engineering in 2024 from Central South University, Changsha, China, where he is currently working toward the Ph.D. degree in control science and engineering.

His research interests include modeling, control, and stability analysis of power electronics converters.

Hanbing Dan (Senior Member, IEEE) was born in Hubei, China, in 1991. He received the B.S. degree in automation and the Ph.D. degree in control science and engineering from Central South University, Changsha, China, in 2012, and 2017, respectively.

He was a visiting researcher with the Faculty of Engineering, University of Nottingham, U.K., during 2017. Since 2018, he has been with the School of Automation, Central South University, Changsha, China, where he is currently an Associate Professor. His research interests include power converter and motor control.

Yao Sun (Member, IEEE) was born in Hunan, China, in 1981. He received the B.S. degree in automation and the M.S. and Ph.D. degrees in control science and engineering from Central South University, Changsha, China, in 2004, 2007, and 2010, respectively.

He has been a Professor with the School of Automation, Central South University, China. His research interests include matrix converters, microgrids, and wind energy conversion systems.

Shiming Xie was born in Fujian, China, in 1995. He received the B.S. degree in electronic engineering and the Ph.D. degree in control science and engineering from Central South University, Changsha, China, in 2017 and 2023, respectively.

Since 2023, he has been a Lecturer with the School of Automation, Central South University. His research interests include matrix converters and modeling and control of power electronics converters.

Wenjing Xiong (Member, IEEE) was born in Hunan, China, in 1991. She received the B.S. degree in automation and the Ph.D. degree in control science and engineering from Central South University, Changsha, China, in 2012 and 2017, respectively.

She is currently an Associate Professor with the School of Automation, Central South University. Her research interests include modulation strategy for matrix converter and ac/dc converters, and wireless power transfer system.

Mei Su (Member, IEEE) was born in Hunan, China, in 1967. She received the B.S. and M.S. degrees in automation and the Ph.D. degree in control theory and control engineering from the School of Information Science and Engineering, Central South University, Changsha, China, in 1989, 1992, and 2005, respectively.

She has been a Full Professor with the School of Automation, Central South University. Her research interests include matrix converter, adjustable speed drives, and wind energy conversion system.

Dr. Su is currently an Associate Editor for IEEE TRANSACTIONS ON POWER ELECTRONICS and IEEE TRANSACTIONS ON SUSTAINABLE ENERGY.